Mon. Not. R. Astron. Soc. **000**, 000–000 (0000) Printed 4 February 2008 (MN LaTeX style file v2.2)

The Three-Point Correlation Function of Luminous Red Galaxies in the Sloan Digital Sky Survey

Gauri V. Kulkarni,[1] Robert C. Nichol,[1,2] Ravi K. Sheth,[3] Hee-Jong Seo,[4] Daniel J. Eisenstein,[4] Alexander Gray[5]
[1] *Dept. of Physics, Carnegie Mellon University, 5000 Forbes Avenue, Pittsburgh, PA 15213, USA*
[2] *Institute of Cosmology and Gravitation, University of Portsmouth, Portsmouth, PO1 2EG, UK*
[3] *Dept. of Physics and Astronomy, University of Pennsylvania, Philadelphia, PA 15105, USA*
[4] *Steward Observatory, University of Arizona, 933 N. Cherry Ave.,Tucson, AZ 85121, USA*
[5] *College of Computing, Georgia Tech, 801 Atlantic Drive, Atlanta, GA 30332, USA*

Accepted . Received ; in original form

ABSTRACT

We present measurements of the redshift-space three-point correlation function of 50,967 Luminous Red Galaxies (LRGs) from Data Release 3 (DR3) of the Sloan Digital Sky Survey (SDSS). We have studied the shape dependence of the reduced three-point correlation function ($Q_z(s, q, \theta)$) on three different scales, $s = 4$, 7 and 10 h^{-1}Mpc, and over the range of $1 < q < 3$ and $0° < \theta < 180°$. On small scales ($s = 4\,h^{-1}$Mpc), Q_z is nearly constant, with little change as a function of q and θ. However, there is evidence for a shallow U–shaped behaviour (with θ) which is expected from theoretical modeling of $Q_z(s, q, \theta)$. On larger scales ($s = 7$ and 10 h^{-1}Mpc), the U–shaped anisotropy in Q_z (with θ) is more clearly detected. We compare this shape–dependence in $Q_z(s, q, \theta)$ with that seen in mock galaxy catalogues which were generated by populating the dark matter halos in large N–body simulations with mock galaxies using various Halo Occupation Distributions (HOD). We find that the combination of the observed number density of LRGs, the (redshift–space) two–point correlation function and $Q_z(s, q, \theta)$ provides a strong constraint on the allowed HOD parameters (M_{min}, M_1, α) and breaks key degeneracies between these parameters. For example, our observed $Q_z(s, q, \theta)$ disfavors mock catalogues that overpopulate massive dark matter halos with many LRG satellites. We also estimate the linear bias of LRGs to be $b = 1.87 \pm 0.07$ in excellent agreement with other measurements.

Key words: methods: statistical – surveys – galaxies: statistics – cosmology: large-scale structure of universe – cosmology: observations

1 INTRODUCTION

The use of correlation functions as probes of the large-scale structure in the Universe has a well established history in cosmology (see Peebles 1980, and references therein). The lowest order correlation function, the two–point correlation function (2PCF), compares the number of pairs of particles (dark matter or galaxies) as a function of their separation, to that expected from a random distribution. It is therefore, an indicator of the strength of clustering. Next in the hierarchy is the three–point correlation function (3PCF), which compares the number of particle triplets, as a function of the triangle shape, to a random distribution. In recent years, with the advent of large galaxy catalogues like the Sloan Digital Sky Survey (SDSS), there has been considerable interest in accurate measurements of the 2PCF and 3PCF. Combining measurements of both 2PCF and 3PCF provides significantly improved constraints on cosmological parameters (Sefusatti et al. 2006).

Measuring the 3PCF is computationally intense as the number of triplets scales as N^3 and thus becomes prohibitive for large samples. In the last few years, optimal algorithms such as NPT (Moore et al. 2001; Nichol et al. 2003; Gray et al. 2004) and similar tree-based algorithms (Szapudi et al. 2001) have been developed, making studies of the higher-order clustering tractable on modern-day computational clusters and grids (Nichol et al. 2005). We use the NPT algorithm in this paper.

In addition, there have been recent improvements in our understanding of the 3PCF (Scoccimarro et al. 2001; Cooray & Sheth 2002;

Takada & Jain 2003; Wang et al. 2004). These are based on the "halo model" approach, which relates the galaxy 3PCF to that of the underlying dark matter. This approach allows measures of the 3PCF to constrain cosmology and galaxy formation models.

Issues of computation and interpretation aside, the measurement itself has been difficult, i.e., previous measurements of the 3PCF have been greatly affected by the presence of rare large–scale structures in the data. For example, Croton et al. (2004), Gaztañaga et al. (2005) and Nichol et al. (2006) have all shown that superclusters present in the the 2dFGRS (Folkes et al. 1999; Colless et al. 2001) and SDSS Data Release One (DR1) can influence the 3PCF significantly on large scales ($\sim 10\ h^{-1}$Mpc). These authors point out the need for samples with large enough volume to "average out" such large–scale structures. The SDSS Luminous Red Galaxy (LRG) sample is well-suited for this purpose as it surveys a volume of $\sim 1\,\mathrm{Gpc}^3 h^{-3}$ (see Figure 1 in Eisenstein et. al. 2005) for the comparison of effective volumes for different surveys.

This paper is organized as follows. In Section 2, we present the sample of LRGs used in our analysis and the measurement of the LRG 3PCF with a full error analysis. In Section 3.2, we discuss our method for preparing mock LRG catalogues, while Section 3.3 contains the measurements of 2PCF and 3PCF from these mock catalogues. We discuss our results in Section 4 and conclude in Section 5. Throughout the paper, we have assumed a ΛCDM cosmology with $\Omega_\Lambda = 0.7$, $\Omega_m = 0.3$ and $H_0 = 100\,\mathrm{km\,s^{-1}\,Mpc^{-1}}$ $(h = 1)$ unless stated otherwise.

2 SDSS DATA AND 3PCF MEASUREMENT

2.1 Data

The Sloan Digital Sky Survey is discussed in a series of technical papers (Fukugita et al. 1996, Gunn et al. 1998, York et al. 2000, Hogg et al. 2001, Stoughton et al. 2002, Strauss et al. 2002, Smith et al. 2002, Pier et al. 2003, Blanton et al. 2003b, Ivezic et al. 2004, Abazajian et al. 2005, Gunn et al. 2006, Tucker et al. 2006). In this paper, we use 50,967 spectroscopically selected LRGs as discussed in detail by Eisenstein et al (2005) and were used to detect and measure the Baryon Acoustic Oscillation peak in the large-scale 2PCF. The details of the LRG selection algorithm are discussed in Eisenstein et al. (2001). Briefly, our sample is based on the SDSS Data Release 3 (DR3) and spans a redshift range of $0.15 < z < 0.55$ with a g-band absolute magnitude range of $-23.2 < M_g < -21.2$. The comoving density is $9.7 \times 10^{-5}\mathrm{Mpc}^3 h^{-3}$, which is approximately constant upto a redshift of $z = 0.36$ and drops thereafter (Eisenstein et. al. 2005). For the calculations of the correlation functions (see Szapudi & Szalay 1998), we use exactly the same random catalogues as Eisenstein et al. (2005), which contain 16 times the number of galaxies as in the real data and have the same selection function as the real data.

2.2 Results of 3PCF measurement

In order to study the dependence of 3PCF on triangle configuration, one needs to parametrize the shape of the triangle. If s_{12}, s_{23}, s_{31} are the lengths of the three sides of a triangle, then a commonly used parametrization is given as (s, q, θ) with $s = s_{12}$, $q = s_{23}/s_{12}$ and θ the angle between s_{12} and s_{23}. Then we can define the reduced 3PCF $(Q_z(s, q, \theta))$, which is the ratio of the 3PCF $(\zeta(s, q, \theta))$, to the sum of the products of the 2PCFs for the three sides (see Groth & Peebles 1977), or

$$Q_z = \frac{\zeta(s, q, \theta)}{\xi(s_{12})\xi(s_{23}) + \xi(s_{23})\xi(s_{31}) + \xi(s_{31})\xi(s_{12})}. \qquad (1)$$

This is also known as the "hierarchical ansatz" (Peebles 1980) and the subscript z denotes measurements made in redshift–space.

One recent issue discussed by Gaztañaga & Scoccimarro (2005; GS05 henceforth) is the effect of binning resolution on the shape of the observed $Q_z(s, q, \theta)$ which potentially hinders our ability to measure the characteristic U-shaped anisotropy (between "open" and "collapsed" triangle configurations) witnessed in N-body simulations (GS05, Fosalba, Pan & Szapudi 2005). The first measurements of the 3PCF from the 2dFGRS (e.g. Gaztañaga et al. 2005) and SDSS (e.g. Nichol et al. 2006) show evidence for this expected U-shaped dependence, but it is not as strong as expected from simulations. Therefore, we measure our $Q_z(s, q, \theta)$ in as narrow bins of s, q and θ as possible. We use $\Delta s = 0.2$ h^{-1}Mpc and $\Delta q = 0.2$ for s and q respectively, while we use $\Delta\theta = \pi/50$, giving potentially 50 bins in θ (we actually only measure the alternate bins in θ, giving 25 in total). Making the θ bins any smaller than this value would lead to very small triangle counts in each bin (i.e. < 10 triplets in some bins), which would then require larger bins in s and q. This binning scheme represents the narrowest set of bins we can construct for our sample of LRGs. However, as demonstrated in Figure 1, this binning scheme is much better than previous measurements and does resolve the shape–dependence of Q_z.

In Figure 2, we show our measurement of the redshift–space reduced 3PCF, $Q_z(s, q, \theta)$, on scales of $s = 4$, 7 and 10 h^{-1}Mpc . We also present these data in Tables A1, A2 and A3 in the Appendix. These scales closely match the s scales used in Figure 2 of GS05 (3, 6 and 12 h^{-1}Mpc respectively in their figure). Measurement of the 3PCF become unreliable on scales less than 4 h^{-1}Mpc because of the small number of triplets in each bin, i.e., we have < 10 triangles. On s scales greater than 10 h^{-1}Mpc , our measurement of the 3PCF from this LRG sample become noisy, e.g., at $s = 18\ h^{-1}$Mpc (a scale used in GS05), it is difficult to detect the shape–dependence in the $Q_z(s, q, \theta)$ given the large error bars (see Figure 3).

2.3 Determination of Errors

The error bars on both the 2PCF and 3PCF were estimated using the jack-knife resampling technique (Scranton et al. 2002; Zehavi et al. 2005). We spilt our sample into 11 (almost) equal area subsets, and then by omitting each of these subsets one-by-one, we repeat the measurement of Q_z eleven times to compute the r.m.s. variation between

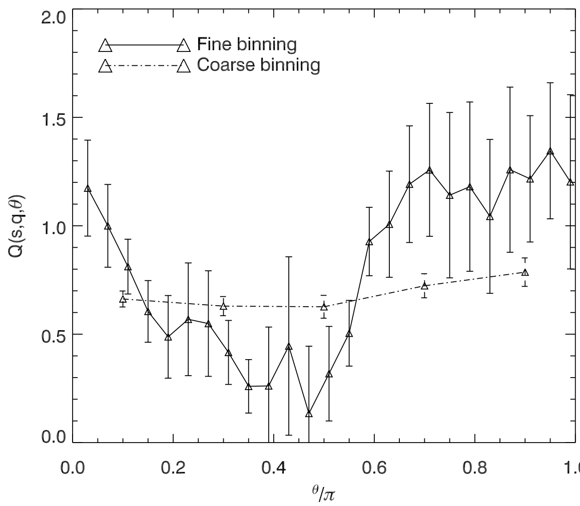

Figure 1. The effect of binning on the shape of the observed $Q_z(s, q, \theta)$. We compare here our measurement for the reduced 3PCF for the triangle configuration of s = 10 h^{-1}Mpc and $q = 2$. Also shown is the coarse binning scheme of Nichol et al. (2006) for the same triangle configuration. Errors on both measurements are from jack-knife resampling (see text for explanation). The coarser (wider) bins tend to "smooth out" features in the $Q_z(s, q, \theta)$ as proposed by GS05.

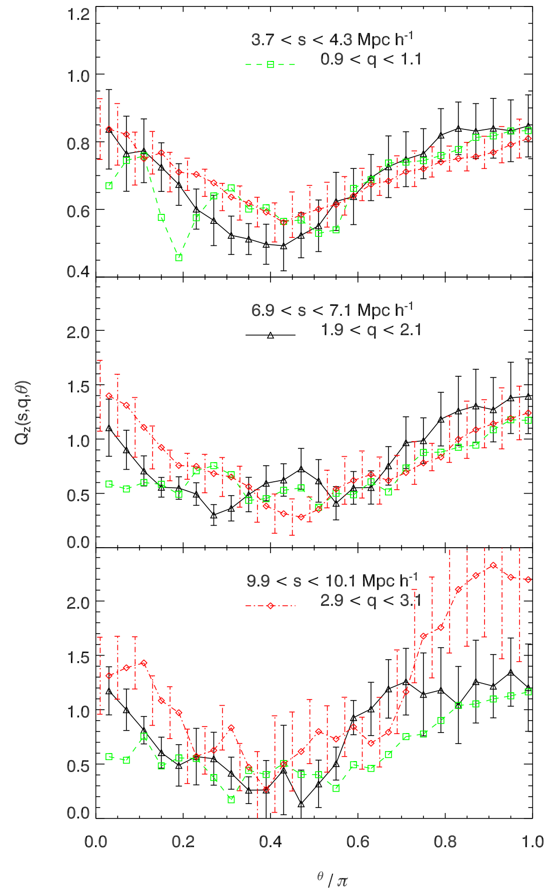

Figure 2. Our measurements of $Q_z(s, q, \theta)$ for three different ranges of triangle scale (s; see label in each panel) and different q values (see all panels for definitions). The dependence of $Q_z(s, q, \theta)$ on the q parameter does not appear to be strong. We do see the gradual emergence of the expected U-shaped behaviour of $Q_z(s, q, \theta)$ going from $s = 4$ to $s = 10$ h^{-1}Mpc. We do not plot the errorbars for $0.9 < q < 1.1$ to avoid overcrowding while errorbars for $2.9 < q < 3.1$ are plotted with an artifical offset of -0.02. Note that the y–axis in the top panel covers a small range of $Q_z(s, q, \theta)$ values than the other two panels. Also, the s ranges shown only apply to the panels they appear in, while the q symbol definitions apply to all three panels

these measurements. This process provides an estimate of the covariance matrix, with the diagonal element of these matrix shown as error bars in our figures. We present in Figure 4 an example of one of our covariance matrices.

One of the advantages of using the jack-knife error technique is demonstrated in Nichol et al. (2006) who used the different $Q_z(s, q, \theta)$ measurements for the different jack-knifes samples to investigate the influence of large–scale structures (e.g. isolated in a single sub–region) on the measurement of the entire sample of galaxies. In Figures 5, 6 and 7 we present the individual measurements of Q_z for the eleven jack–knife samples for the three scales, i.e., $s = 4$, 7 and 10 h^{-1}Mpc. The first three panels of Figures 5, 6 and 7 show the absolute value of the percentage difference between the individual eleven jack-knife measurements compared to the measurement from the whole LRG sample. These panels demonstrate that there is no single "rogue" sub–region that dominate the error on the 3PCF, unlike the findings of Nichol et al. (2006) that found the 3PCF of the SDSS main galaxies was dominated by the presence of the "Sloan Great Wall".

The last (lower right) panel of Figures 5, 6 and 7 compare our estimation of the errors on $Q_z(s, q, \theta)$ for the whole LRG sample with the expected Poisson error for the number of triplets in each bin. For the 4 and 7 h^{-1}Mpc scales, the Poission errors are approximately the same as the jack–knife errors indicating that on these scales the main source of error is simply shot–noise. Therefore, bigger samples of LRG galaxies will improve the measurement of the 3PCF on these small scale. However, in Figure 7 (right panel), we see a different behavior, with the jack–knife errors being three times larger than the Poission errors. This demonstrates that on these larger scale the correlation function bins are highly correlated by the large-scale structure in the Universe. The stability of the jack–knife errors on these large scales ($s = 10$ h^{-1}Mpc) also confirms that the jack–knife technique has captured such correlations between the bins and is a better measure of the true error on these scales.

3 CORRELATION FUNCTIONS OF MOCK CATALOGUES

3.1 The Halo Model

We use mock catalogs based on the halo model to interpret our measurements of the LRG 3PCF. Briefly, let $p(N|M)$ denote the probability that a halo of mass M contains N LRGs. The first moment of this probability distribution,

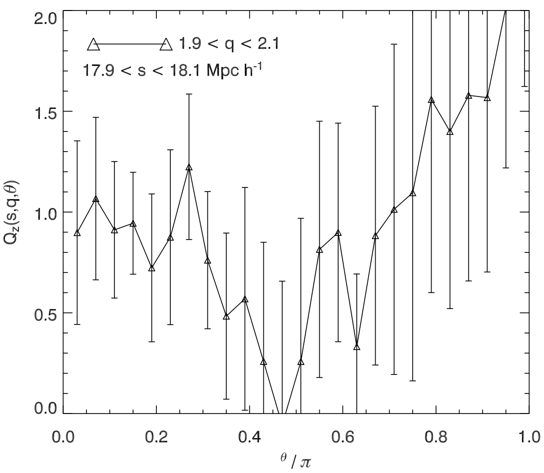

Figure 3. The measurement of $Q_z(s, q, \theta)$ on large scales, i.e., $s = 18\ h^{-1}$Mpc. The errors on this measurement are large, making it hard to unambiguously detecting any shape–dependence. The solid black line (with triangle symbols) is the measurement of $Q_z(s, q, \theta)$ with the same bins as used in Figure 2.

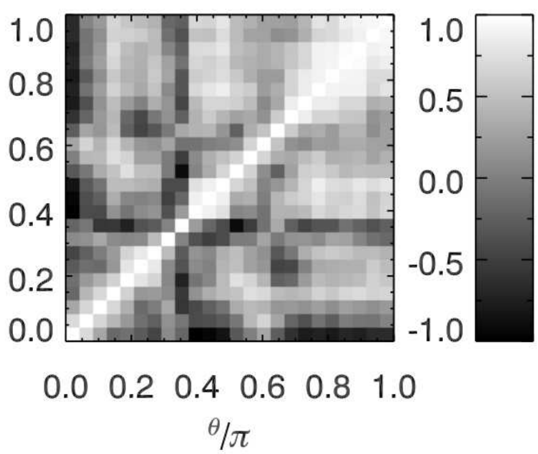

Figure 4. We present here the normalized covariance matrix for the 3PCF for the triangle configuration of $9.9 < s < 10.1\ h^{-1}$Mpc with $1.9 < q < 2.1$. See Figure 7 for further explanation.

$\langle N|M\rangle$, gives the mean number of LRGs in a halo of mass M; it is sometimes called the Halo Occupation Distribution (HOD). We use the following parameterized form for this relation:

$$\langle N_{cent}(M)\rangle = \exp\left(-\frac{M_{min}}{M}\right), \quad (2)$$

$$\langle N_{sat}(M)\rangle = \exp\left(-\frac{M_{min}}{M}\right)\left(\frac{M}{M_1}\right)^{\alpha}, \quad (3)$$

$$\langle N(M)\rangle = \langle N_{cent}(M)\rangle + \langle N_{sat}(M)\rangle\,. \quad (4)$$

The terms central and satellite have the following meanings. In halos which host more than one LRG, the first LRG is placed at the halo center and is called the central galaxy; the others are distributed around this center and are called satellites. The expressions above show that there is assumed to be a reasonably sharp mass threshold M_{min} below which halos are increasingly (exponentially) unlikely to host even one (central) LRG. More massive halos which host a central LRG may also host satellites, the typical number of which is assumed to scale as a power law in halo mass: M_1 denotes the mass required to host at least one satellite, and the slope of the power law, α, describes how quickly the mean number of satellites increases with mass. Zehavi et al. (2005) have shown that this parametrization, with $M_1 \approx 23M_{min}$ and $\alpha \approx 1$ provides a good desription of the HOD for galaxies above some threshold luminosity in the SDSS Main Galaxy Sample (M_{min} increases with increasing threshold luminosity).

The expressions above specify only the mean of $p(N|M)$. When inserted into the halo model, this is only sufficient to estimate the mean number density of LRGs. To predict the 2PCF, a model for the second moment of this distribution is required; the third moment of $p(N|M)$ is required for the 3PCF. We specify the entire hierarchy of correlation functions by assuming that the number of satellites in a halo which contains a central LRG is drawn from a Poisson distribution with mean $N_{sat}(M)$. This Poisson satellite assumption is motivated by results in Kravtsov et al. (2004), and was used by Zehavi et al. (2005) in their study of the luminosity dependence of the 2PCF in the SDSS Main Galaxy Sample.

3.2 Mock Catalogues

We begin with dark matter halo catalogues generated from a set of six cosmological N-body simulations with a box size of $512^3(\mathrm{h}^{-1}\mathrm{Mpc})^3$, containing 256^3 particles of mass $8.28\times10^{11}\ M_\odot$. The N-body simulations are generated using the Hydra code (Couchman et al. 1995) in collisionless particle-particle-particle-mesh ($\mathrm{P^3M}$) mode with 256^3 force grids and a Plummer softening length of $0.2h^{-1}$Mpc (see Seo & Eisenstein 2005 for more details about these simulations). The cosmological parameters used to generate the simulation are $\Omega_m = 0.27$, $\Omega_\Lambda = 0.73$, $h = 0.72$, $\sigma_8 = 0.9$ and $n = 0.99$, in agreement with the WMAP1 best–fit values. Halos in these simulations were detected using the friends-of-friends algorithm (Davis et al. 1985) with a linking length of $0.6h^{-1}$Mpc and a minimum group multiplicity of 20 particles. We note that these simulations do not use the more conventional $b = 0.2$ linking length and therefore, our halo masses will exceed the halo masses from more conventional simulations (e.g. which are closer to M_{200}). We have checked that our mass functions are approximately the same as the Sheth & Tormen (1999) $z = 0$ mass function but with all the masses scaled by 1.5. Our mass functions can therefore be thought of as representing the expected mass functions in the near future and, at a fixed number density, we would not expect the HOD for these massive LRGs to have evolve significantly. This should make comparisons with other HODs in the literature easier, but such issues should be taken into account when performing detailed comparisons with our best–fit M_{min} and M_1 values, although α should not be different[1].

[1] To facilitate a detailed comparison with our HOD results, the mass functions of our simulations are available on request.

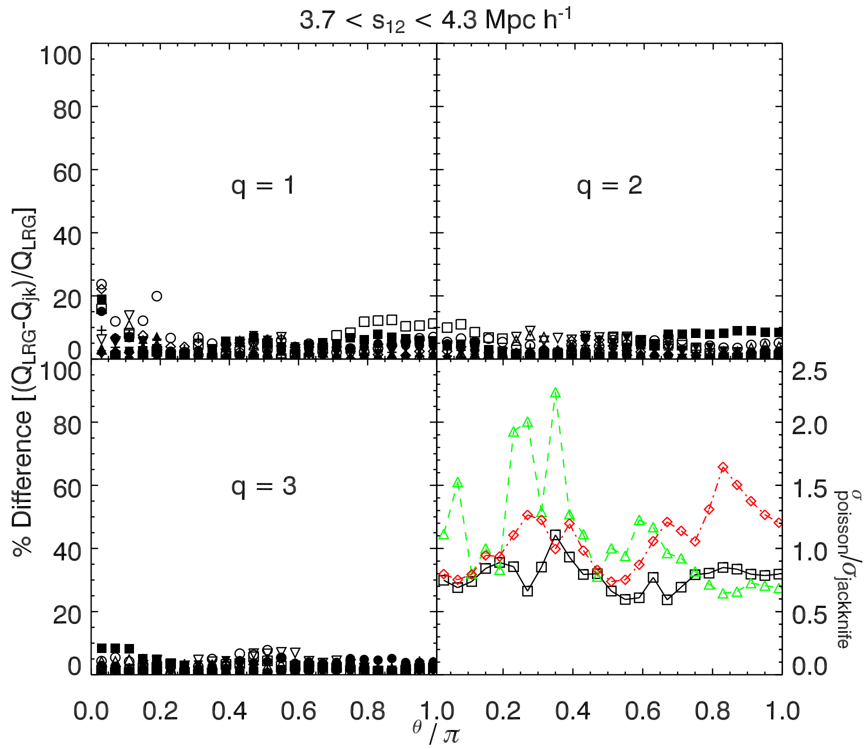

Figure 5. The absolute percentage difference between the 3PCFs of the 11 jack-knife datasets discussed in the text and the full dataset for the $s = 4\ h^{-1}$Mpc scale (first three panels). No single jack-knife estimation dominates the difference between these measurements, thus indicating the LRG sample is a fair sample of the Universe on this scale. Last panels (lower right) shows the comparison of the errors with the expected Poisson errors. The green triangles are for q = 1, black squares are for q = 2 and red diamonds are for q = 3.

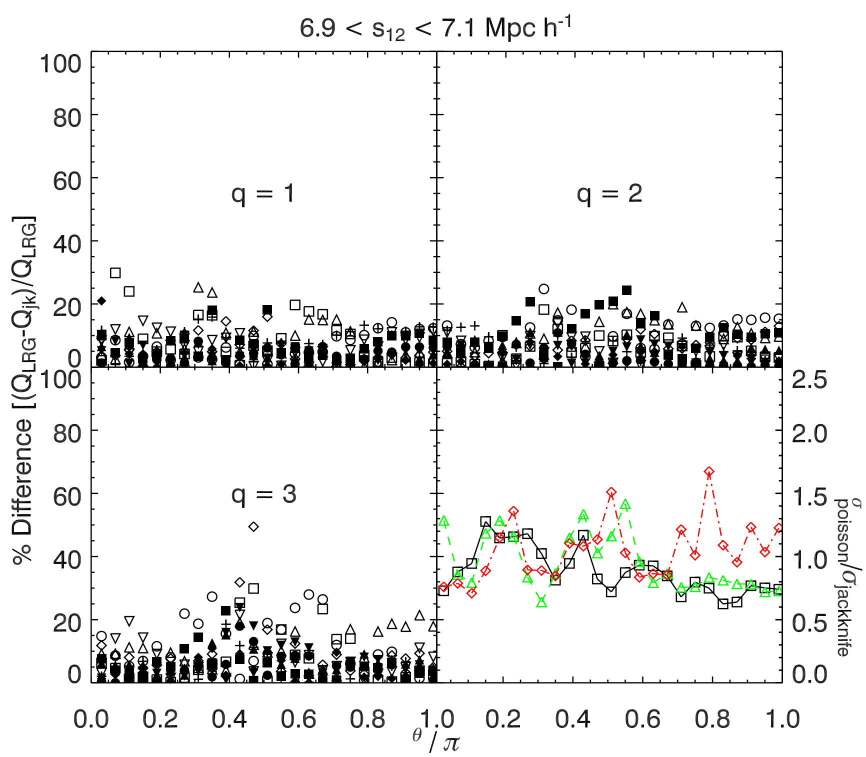

Figure 6. The same as Figure 5, but for the scale $s = 7\ h^{-1}$Mpc scale.

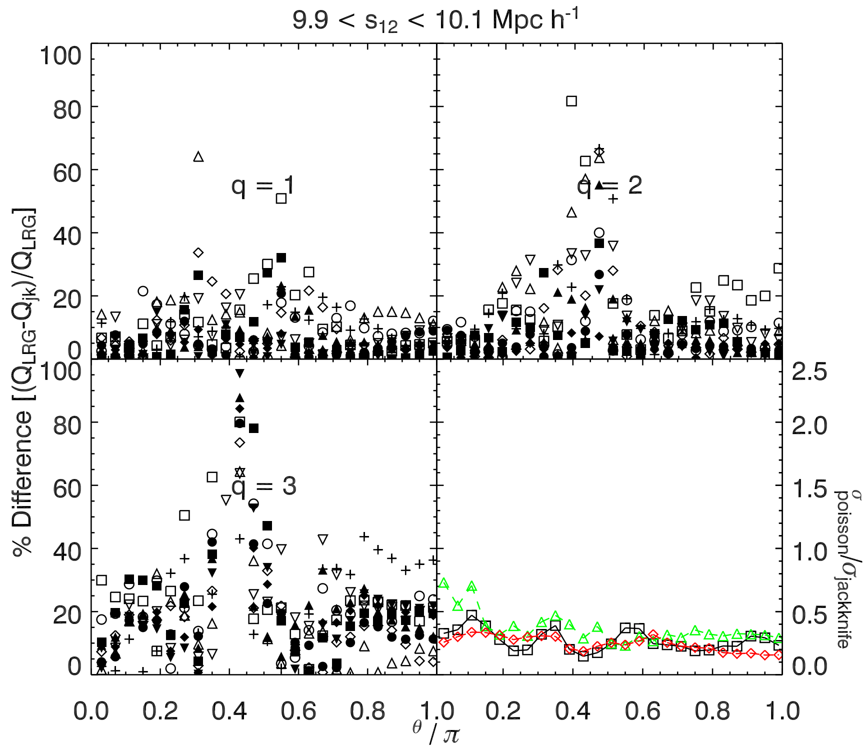

Figure 7. The same as Figure 5 but for the $s = 10\ h^{-1}$Mpc scale. However, on this scale, although no single jack–knife region dominates, there is considerably larger variations between the different regions. Also, the jack-knife errors are now significantly larger than the expected Poisson errors (as indicated in the lower right panel), which indicates the errors are correlated on these larger scales as expected because of large-scale structures in the Universe.

Initially, we use a halo catalogue generated from one of the six simulations, henceforth called the *parent* simulation, and then use the halo model to populate the dark matter halos in the simulations with central and satellite LRGs. The halo model has three free parameters, and so we construct mock catalogs which have a range of M_{min}, M_1 and α. Specifically, M_{min} spans the range from the minimum halo mass in the simulation (called M^{sim}_{min}) to the maximum halo mass (called M^{sim}_{max}) in the simulation using integer steps of the value of $1\times10^{13} M_{\odot}$. By varying M_1 from M_{min} to M^{sim}_{max} in the steps of M^{sim}_{min}, we also find a range of M_1 values for each M_{min}. As N_{sat} in Eqns 2 & 3 changes slowly over this range, we sample it in logarithmic steps of 0.1. Using the value of M^{sim}_{min} to increment M_1 assures we have a reasonably fine grid of models to test against the observations. The slope α was allowed to vary from 0.9 (the value obtained by Zehavi et al. (2005) for their faintest galaxy sample) to 4 in increments of 0.1.

We compute the mean number of galaxies associated with each HOD and reject those cases in which the associated number density differs by more than 5% from the observed mean density of LRGs in our sample (this latter was estimated from a volume–limited subsample). Eisenstein et al. (2005) show that the comoving density is constant for the redshift range $0.16 < z < 0.36$. Only 354 different combinations of HOD parameters survive this test.

For each of the 354 allowed set of HOD parameters, we populate the dark matter halos in the simulations as follows. We bin all halos into 300 equal mass bins between M^{sim}_{min} and M^{sim}_{max}. If N_i denotes the number of halos in the

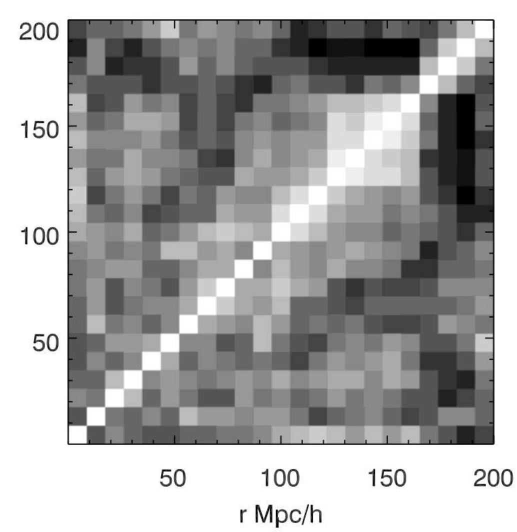

Figure 8. Covariance matrix for 2PCF measurement of the LRGs. The colour scheme is same as in figure 4.

ith bin, then we choose $N_i \exp -(M_{min}/M_i)$ halos at random from N_i and assign them a central LRG. The central LRG is assigned the same spatial coordinates as the center of mass of its host halo. For halos which host a central LRG, the number of satellite LRGs was drawn from a Poisson distribution with mean given by Eqn 3. The positions of these satellite LRGs were assigned using the NFW

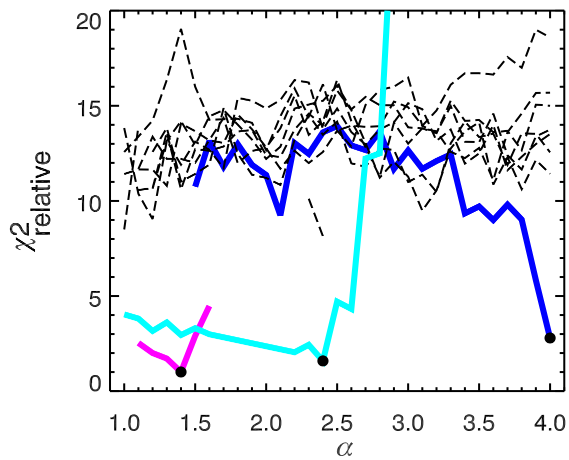

Figure 9. We present here slices in χ^2–space (we have normalized these curves by the minimum χ^2 of all the 354 mocks). Each curve corresponds to a unique set of M_{min} and M_1 combinations, as a function of α. The thick, coloured curves are the three preferred solutions discussed in the text. The solid black circles on each of the solid curves corresponds to the solution chosen from that group for the analysis in this paper. We note that some of the curves do not span a full range of α values because these combinations of the three HOD parameters have been excluded by our initial number density constraint, e.g., the magenta curve. Also, curves with parameters that yield (normalized) $\chi^2 > 60$ are not plotted here.

(Navarro, Frenk & White 1997) density profile. Since our measurements are in redshift space, we must also model the peculiar velocities of our mock LRGs. We work in the "distant observer approximation", meaning that redshift space effects are incorporated by adding peculiar velocities to the z-components of the position vectors of the mock galaxies. This was done as follows. The central LRG in a halo is assumed to have the same velocity vector as its host, so redshift space distortions are due to the z-component of the halo's velocity vector, v_z. The satellites are assumed to be in approximately virial equilibrium; to model this, the velocity of a satellite is given by adding a random Gaussian number with rms $\sigma_z \propto M_{halo}^{1/3}$ to v_z before combining with the z-component of the spatial position (Sheth & Diaferio 2001). We populate the halos of the other five simulations using the set of allowed HOD parameters derived from the *parent* simulation (only the *parent* simulation satisfies the number density constraint discussed above, while the other five mocks can violate this constraint). Thus, for each allowed set of HOD parameters, we have six mock catalogues all in redshift–space.

3.3 Testing the Mocks

In this section, we compare our mock catalogues with the real SDSS data. Using the same initial simulation as discussed in Section 3.2, we measure the 2PCF for each of the 354 allowed mocks. We then define a χ^2 from the difference between the 2PCF measured in the mock and the real data, over the range $0.89 < s < 57\ h^{-1}$Mpc (corresponding to 18 bins in separation). For this comparison, we use the full covariance matrix obtained for the real data (Figure 8) using 20 jack-knife sub–samples (instead of 11). We have used more jack-knife regions here than for the 3PCF above (see Section 2.2), as it provides a more stable inversion of the covariance matrix on small scales ($0.89 < s < 9\,h^{-1}$Mpc).

Figure 9 shows individual slices through the (normalised) χ^2 surface as defined by the M_{min} and M_1 HOD parameters for the 354 allowed mock catalogues. As can be seen, there are 3 distinct curves (or "valleys") in this 3D parameter space of M_{min}, M_1 and α that possess the three lowest minima in the χ^2 surface. These three curves are highlighted (in colour) in Figure 9 and have the values of $M_{min} = 7.66 \times 10^{13} M_\odot,\ M_1 = 4.7 \times 10^{14}$ (magenta); $M_{min} = 7.66 \times 10^{13} M_\odot,\ M_1 = 7.6 \times 10^{14} M_\odot$ (cyan); and $M_{min} = 6.66 \times 10^{13} M_\odot,\ M_1 = 1.3 \times 10^{15} M_\odot$ (blue). In Figure 10, we show the mean and rms variation (from the six mocks) for both the 2PCF and 3PCF for these three sets of HOD parameters with the lowest χ^2 values shown in Figure 9. Table 1 provides the best fit HOD parameters.

4 DISCUSSION

In Figure 2, we show the shape dependence of the reduced 3PCF ($Q_z(s, q, \theta)$) for the Luminous Red Galaxy sample presented in Eisenstein et al. (2005). On small scales ($3.7 < s < 4.3h^{-1}$Mpc), our $Q_z(s, q, \theta)$ is nearly constant for all values of q (consistent with the original findings of Groth & Peebles 1977). There is however clear evidence for a shallow U–shaped anisotropy between "open" triangles (defined to be triangle configurations at the ends of the θ range) and "collapsed" trianges (configurations with intermediate θ values). The absence of a strong U-shape, especially at the ends of the θ range, suggests the lack of strong "Fingers–of–God" (FOG) for these LRGs, which is to be expected as many halos only possess one, or a few, LRGs. For example, approximately 50% of cluster-size halos in our mocks (masses of $> 10^{14}\ M_\odot$) only have a single LRG. This can be contrasted to the sharp U–shaped behaviour (at $\theta \simeq 0$ and $\theta \simeq 180$ degrees) on small scales seen in the dark matter simulations of GS05.

On larger scales ($s = 7$ and $s = 10\ h^{-1}$Mpc), the broad U–shaped anisotropy of the reduced 3PCF becomes more pronounced, due to the emergence of the large–scale filamentary structure in the Universe. This is now in qualitative agreement with earlier results (Frieman & Gaztanaga 1999) and expectations from N–body simulations (but still less than predicted, on these scales, by GS05). A more detailed comparsion of the observed 3PCFs and dark matter simulations will be required and is beyond the scope of this paper.

Throughout this paper, we have used the same 3PCF parametrization of the triangle configurations as GS05 (s,q,θ) to allow for easy comparison with their work and other recent measurements of the 3PCF (Gaztanaga et al. 2005; Nichol et al. 2006). However, we note that this parametrization can lead to some triangles being represented more than once in different bins. We have not corrected for this effect here but stress that our jack–knife errors will include any extra correlations due to this effect. This may explain some of the significant off-diagonal elements in the

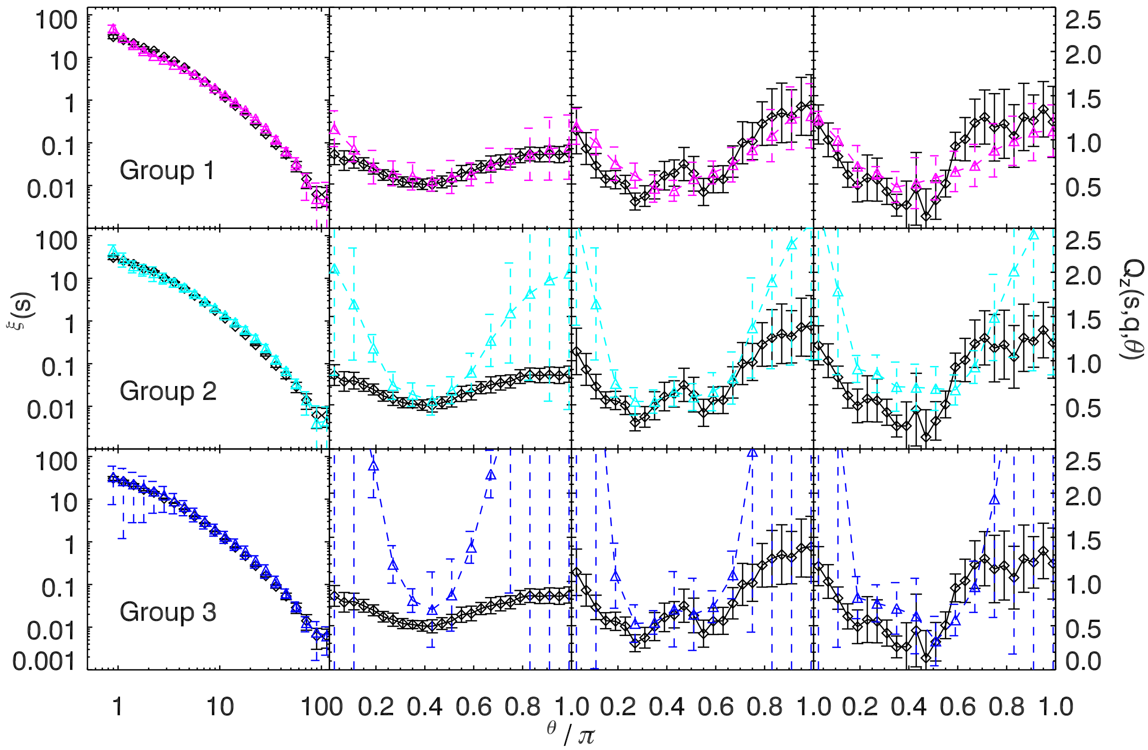

Figure 10. We present the 2PCF and 3PCF of the mock LRG catalogues from three "best" mocks discussed in the text, i.e., the three mock catalogues with the lowest χ^2. The colour scheme follows the same one used in Figure 9. For each row, from left to right, we show the measurements of the 2PCF (both mock and real data), the 3PCF at the scale $3.7 < s < 4.3$ h^{-1}Mpc, the 3PCF at the scale $6.9 < s < 7.1$ h^{-1}Mpc and the 3PCF at the scale $9.9 < s < 10.1$ h^{-1}Mpc. For the 3PCF, we only show the $1.9 < q < 2.1$ bin. The measurements for the mocks are the mean and variance over the 6 simulations available to us. In each group, we see excellent agreement between the 2PCF of the mocks and real data. However, 3PCFs behave very differently.

covariance matrices (Figure 4). We note that our mock catalogues have been analysed in the exact same way as the real data and therefore, also include such issues. We also use the narrowest bins possible in s,q and θ, which will minimize this effect and keep the bins as independent as possible.

Instead, we have used the halo model to understand the LRG 3PCF in redshift–space. We have used dark matter halos from large N–body simulations to create mock galaxy catalogues which are tested against the real data using both their mean number density of galaxies and 2PCF. We find that our mock catalogues fall into three distinct groupings (which possess the lowest χ^2 fits to the real data) as defined by their HOD parameters (M_{min}, M_1, α). In reality however, our 2PCF fits (in Section 3.3), are insensitive to M_{min} (the minimum mass of a halo to hold a central galaxy) because it is initially constrained by our requirement on the number density of LRGs. Therefore, only M_1 and α are allowed to change and as demonstrated in Figure 10 (first column) there are multiple combinations of these two parameters that give good fits to the 2PCF. Figure 9 clearly shows the degeneracy between M_1 and α. However, Figure 10 demonstrates that the 3PCF can break this degeneracy between these parameters as the $Q_z(s, q, \theta)$ from the mocks changes significantly as M_1 and α are varied (while the 2PCF remain almost identical).

It is worth discussing here the size of the error bars on our $Q_z(s, q, \theta)$ measurements for the mocks (i.e., the variance between the 6 mock catalogues used herein) shown in Figure 10. In particular, the error bars for Groups 2 & 3 in Figure 10 are significantly larger than those for Group 1 and are caused by two of the six dark matter simulations having significantly more massive halos than the other four. This is illustrated in Figure 11. We denote these two "rogue" simulations as *sim1* and *sim2*, and if we omit these two simulations when computing the mean and variance, then our fits to the 2PCFs and 3PCFs are significantly better with smaller errors, see Figure 12 (columns 2, 3 and 4).

To understand this further, we show in Figure 13 a 50 h^{-1}Mpc thick slice for one of our mock galaxy catalogues generated using the *sim1* simulation and using the Group 3 HOD parameters shown in Figures 10 and 12. As expected with such a high value of α in the HOD, the most massive halos in the mass function become heavily populated with satellite LRGs and therefore, produce very strong FOG (along the z-direction). This is clearly not realistic.

We also note that in the case of Group 3 in Figure 12, the agreement between the real and mock 2PCF has decreased on small scales. This is due to the removal of the heavily populated mass halos in *sim1* and *sim2*, which mostly affect the 1-halo term, leaving the 2-halo term (on quasi-linear to linear scales) unaffected because it is fixed by the initial number density constraint set on these mock cat-

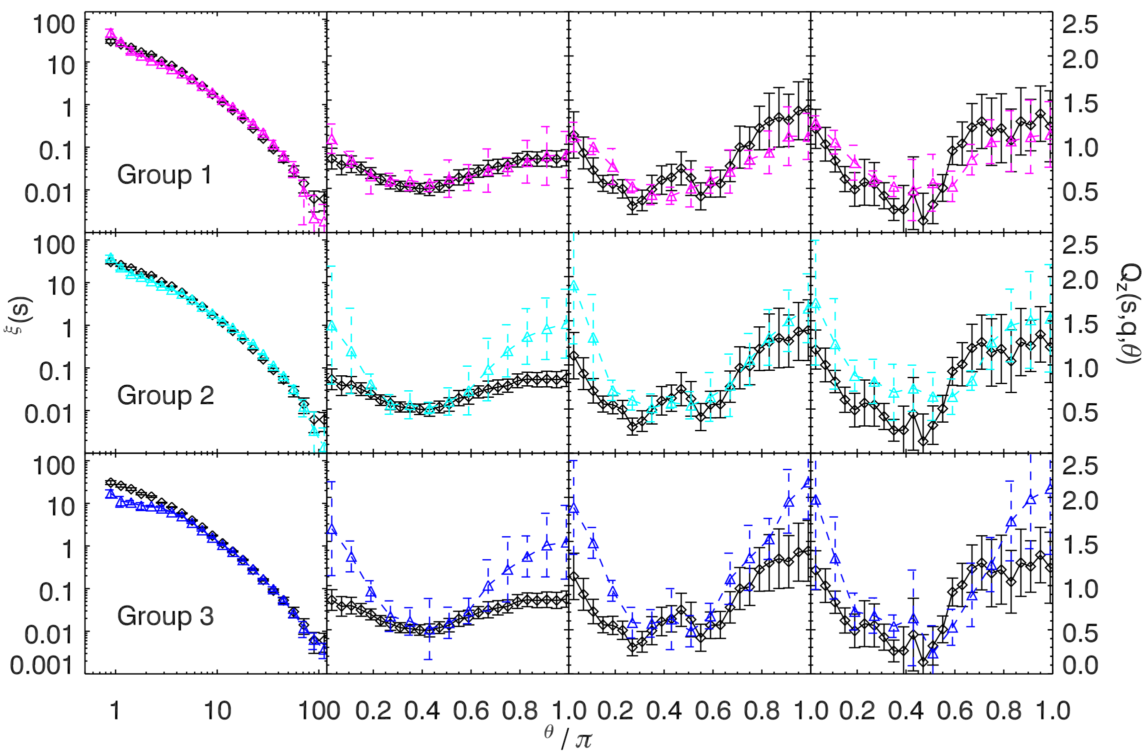

Figure 12. The same as Figure 10, but with *sim1* and *sim2* excluded (shown in red in Figure 11). Even after omitting these two simulations, the 2PCF of the mocks and data are still in good agreement. For the 3PCF, we still witness more anisotropy in the mocks for the bottom two mocks than observed in the data.

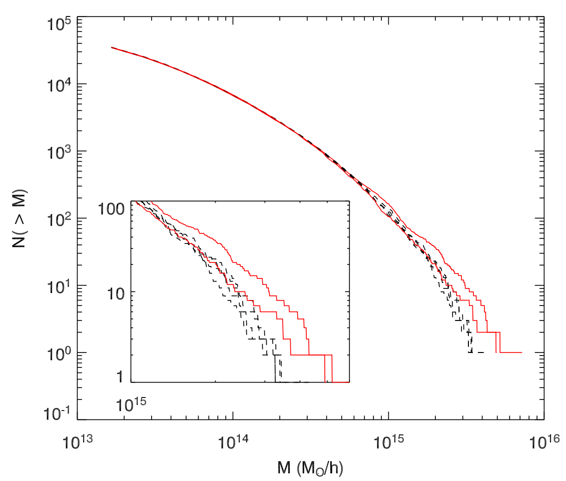

Figure 11. The number of halos, greater than a given mass M, for six simulations used in this paper. The functions shown in red are the two simulations excluded in Figure 12 and discussed in the text.

alogues, i.e., the number density constraint imposes a mass threshold for the halos which contain a central galaxy, which in turn, sets the threshold for the mass peaks that can enter into the 2–point calculation.

This work demonstrates the degeneracy between the M_1 and α HOD parameters and how one can overpopulate the most massive halos to compensate for an increase in the M_1 parameter, the mass threshold for adding satellite galaxies to halos. This is clearly illustrated in the three best–fit parameterized HODs presented in Figure 14. All three HOD models have approximately the same minimum χ^2's (in Figure 9), and approximately the same M_{min} (because of the constraint on the number density). Clearly, as one increases M_1, the slope of the HOD must increase to compensate.

In summary, this work shows that one needs both the 2PCF and 3PCF to break degeneracies in the HOD parameters, especially M_1 and α. We also show in Figure 10 that our 3PCF analysis favors HOD models with low values of α, i.e., it prefers to populate lower mass halos with satellites at the expense of overpopulating massive, cluster–like halos with many satellites. This result agrees with Collister & Lahav (2005), who find $\alpha \sim 1$ for the HOD of red galaxies in clusters and groups of galaxies detected in the 2dFGRS (see also Popesso et al. 2006).

This work provides an important insight into the LRG population and indicates that LRGs are optimal tracers of massive dark matter halos as there is at least one LRG per halo all the way down to $M_{halo} \simeq 10^{14} M_\odot$ (see Figure 14). Therefore, by combining the mean observed number density, 2PCF and 3PCF, and using the halo model to understand how LRGs populate massive halos, one should be able to accurately test the underlying cosmological parameters and assumptions of gaussianity. For example, one can test a suite of different cosmological simulations (by

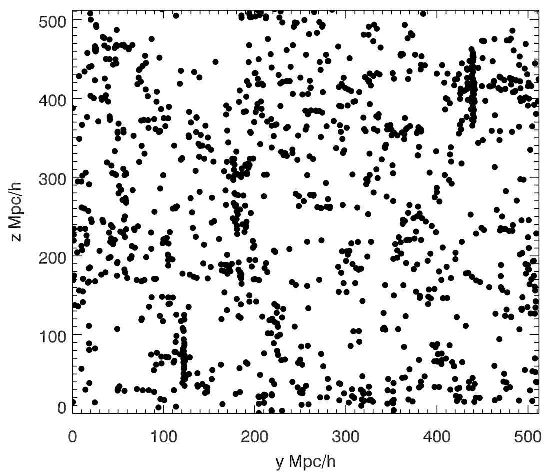

Figure 13. We present a 50 h^{-1}Mpc slice through our mock catalogue with large 3PCF. Very large "fingers–of–god" are visible e.g. at y ≈ z ≈ 450 h^{-1}Mpc.

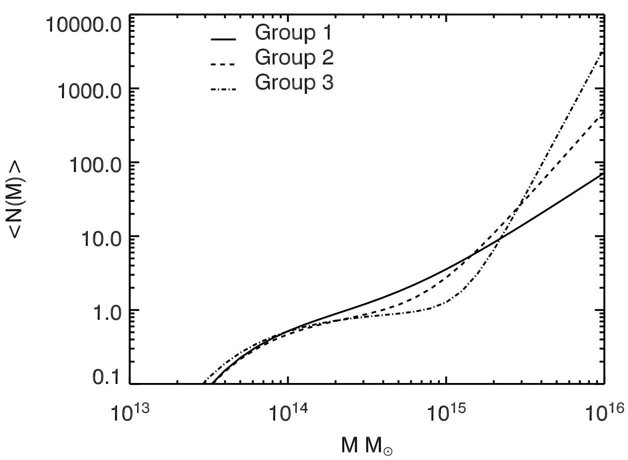

Figure 14. We show here the three HODs ($\langle N(M)\rangle$) with the lowest 3 χ^2 values shown as black dots in Figure 10.

varying parameters like σ_8, Ω_m etc.) against the data, and using the 3PCF to constrain the HOD parameters, while the large–scale 2PCF would be sensitive to the changes in the cosmology (Zheng & Weinberg 2005). It is therefore reassuring that our present best–fit mock catalogue (shown in the top row of Figure 10) provides an excellent fit to all the data presented in this paper, as it is derived from numerical simulations based on the WMAP1 cosmological parameters (Spergel et al. 2003) and assumed gaussian initial conditions. Clearly as the data and mock catalogues improve, we can investigate these issues further and will explore them in future papers.

Finally, in this paper we have focused on the halo model interpretation of the higher–order LRG clustering rather than the more established "biasing" model for relating dark matter to galaxies (see Verde et al. 2002, Gaztanaga et al. 2005, Marin et al. 2006). We plan to explore galaxy biasing in detail in a separate paper (e.g. Nishimichi et al. 2006) using the LRG 3PCF presented in this paper and dark matter simulations. However, we can obtain some insight into linear biasing (even in redshift–space, see Nishimichi et al. 2006) (b) using the simulations published by GS05. For example, the top right–hand panel of Figure 2 of GS05 shows that the redshift–space $Q_z(s,q,\theta)$ for dark matter is close to unity for $30^\circ < \theta < 150^\circ$ (their ΛCDM 400 simulation is close to the simulations used herein and our assumed cosmology). Therefore, we fit the observed $Q_z(s,q,\theta)$ for the $s = 7$ h^{-1}Mpc scale with a constant over the same range of θ values and obtain 0.55 ± 0.04. This value is relatively insensitive to the exact θ range fitted and demonstrates that a constant is a good approximation to the form of $Q_z(s,q,\theta)$ within this θ–range. Assuming linear bias, then $b \simeq Q_z^{DM}/Q_z^{observed}$, which gives $b = 1.83 \pm 0.07$ assuming $Q_z^{DM} = 1$. This confirms our expectation that LRGs are heavily biased (with respect the the dark matter) and our measured linear bias value is in excellent agreement with the analysis of Zehavi et al. (2005), who measured $b = 1.84 \pm 0.11$ (on scales $1 < r_p < 10$ h^{-1}Mpc) from the projected 2PCF of the same LRG sample.

5 CONCLUSIONS

We present in this paper new measurements of the redshift-space three-point correlation function of LRGs from the Sloan Digital Sky Survey (see Figure 2). We have used the same sample as presented in Eisenstein et al. (2005) and Zehavi et al. (2005) who studied the two–point correlations function of these LRGs. The major conclusions of our work are:

- We see strong evidence for the expected U–shaped anisotropy in the shape–dependence of the reduced 3PCF, $Q_z(s,q,\theta)$, as a function of θ (the angle between two sides of the triangle). The evidence is weakest on the smallest scales probed here ($s = 4$ h^{-1}Mpc), where $Q_z(s,q,\theta)$ is close to a constant as a function of both q and θ. We therefore we are not seeing strong "Fingers–of–God" for LRGs as few LRGs are satellite galaxies. On larger scales, a U–shaped anisotropy is predicted (from perturbation theory) and we see evidence for such large–scale structures in our LRG sample.
- We use jack–knife re–sampling to measure the errors on Q_z and find these errors are stable on all scales to which we are sensitive. We find that no single jack–knife region dominates the errors, in contrast to previous measurements of the 3PCF (Croton et al. 2004, Nichol et al. 2006). On small scales ($s = 4$ and 7 h^{-1}Mpc), our jack-knife errors are equal to the expected Poisson errors (based on the number of triplets in each bin), while for the $s = 10$ h^{-1}Mpc scale, our errors are approximately three times larger than Poisson, indicating they are correlated due to large–scale structures.
- We interpret the observed $Q_z(s,q,\theta)$ using a suite of mock galaxy catalogues generated from large N–body simulations and populated with galaxies using the "halo model" approach, i.e., we use a parameterized Halo Occupation Distribution (HOD) to assign LRGs to the dark matter halos. We find that the combination of the observed number density of LRGs, the (redshift–space) two–point correlation function and $Q_z(s,q,\theta)$ provides a strong constraint on the

Table 1. The best-fit HOD parameters for the three groups in Figure 9. Masses are given in $M_{\odot}$. SF and ρ are the average satellite fraction and average number density across the mocks from the six simulations respectively, while σ_{SF} and σ_{ρ} are the respective errors. The numbers in the bracket are the averages across the mocks exlcuding the rogue simulations.

Group	M_{min}	M_1	α	SF	σ_{SF}	ρ	σ_{ρ}
1	7.66 $\times 10^{13}$	4.7 $\times 10^{14}$	1.4	17.4 (17.3) %	0.70 (0.21)	$1.02 \times 10^{-4}(1.01 \times 10^{-4})$	0.014 (0.005)
2	7.66 $\times 10^{13}$	7.6 $\times 10^{14}$	2.4	10.0 (9.23) %	1.64 (0.37)	$9.34 \times 10^{-5}(9.19 \times 10^{-5})$	0.023 (0.006)
3	6.66 $\times 10^{13}$	1.3 $\times 10^{15}$	4.0	4.63 (3.24) %	2.49 (0.26)	$1.03 \times 10^{-4}(1.00 \times 10^{-4})$	0.038 (0.005)

allowed HOD parameters (M_{min}, M_1, α) and breaks key degeneracies between M_1 and α, the mass threshold for adding a satellite LRG and the slope of the power law for the satellite fraction (Eqns 2 & 3).

• The best–fit mock galaxy catalogue to all the data presented in this paper has HOD parameters of $M_{min} = 7.66 \times 10^{13} M_{\odot}$, $M_1 = 4.7 \times 10^{14}$ and $\alpha = 1.4$ (see Eqns 1 & 2, and Figure 10). Furthermore, we find our $Q_z(s, q, \theta)$ strongly rejects HODs with higher values of α as they overpopulate the massive halos leading to stronger "Fingers–of–God" than witnessed in the real data (see Gaztañaga & Scoccimarro 2005). As shown in Table 1, only 17% of LRGs are satellite galaxies.

• Assuming linear biasing between the dark matter and LRGs on the scales probed here, we estimate $b = 1.83 \pm 0.07$ (assuming $Q_z^{DM} = 1$). This value is in excellent agreement with Zehavi et al. (2005) based on the projected 2PCF of the same LRG sample.

To facilitate further analysis of the LRG sample, the 2PCF, 3PCF, mass functions and covariance matrices presented in this paper are available on request from Bob Nichol and/or via the website `http://www.dsg.port.ac.uk/~nicholb/3pt/kulkarni/` .

ACKNOWLEDGMENTS

We thank the referee for the comments. We thank Rupert Croft, Peder Norberg, Kathy Romer, David Weinberg, Larry Wasserman and Zheng Zheng for stimulating conversations and important insights about our work. We thank Quentin Mercer III, Rupert Croft and Albert Wong for their help and assistance in building and maintainace of astrophysics Beowulf Cluster at Carnegie Mellon University. We also thank the administrators of TeraGrid at NCSA for their help in running 3PCF on the NCSA supercomputer. The work presented here was partially funded by NSF ITR Grant 0121671. RN also thanks the EU Marie Curie program for partial funding during this work.

Funding for the SDSS and SDSS-II has been provided by the Alfred P. Sloan Foundation, the Participating Institutions, the National Science Foundation, the U.S. Department of Energy, the National Aeronautics and Space Administration, the Japanese Monbukagakusho, the Max Planck Society, and the Higher Education Funding Council for England. The SDSS Web Site is http://www.sdss.org/.

The SDSS is managed by the Astrophysical Research Consortium for the Participating Institutions. The Participating Institutions are the American Museum of Natural History, Astrophysical Institute Potsdam, University of Basel, Cambridge University, Case Western Reserve University, University of Chicago, Drexel University, Fermilab, the Institute for Advanced Study, the Japan Participation Group, Johns Hopkins University, the Joint Institute for Nuclear Astrophysics, the Kavli Institute for Particle Astrophysics and Cosmology, the Korean Scientist Group, the Chinese Academy of Sciences (LAMOST), Los Alamos National Laboratory, the Max-Planck-Institute for Astronomy (MPIA), the Max-Planck-Institute for Astrophysics (MPA), New Mexico State University, Ohio State University, University of Pittsburgh, University of Portsmouth, Princeton University, the United States Naval Observatory, and the University of Washington.

REFERENCES

Abazajian, K., et al. 2005, AJ, 129, 175
Blanton, M. R., et al. 2003, AJ, 125, 2348
Bullock, J. S. et al, 2001, MNRAS, 321, 559
Colless, M. et al, 2001, MNRAS, 328, 1039
Collister, A. A, Lahav, O., 2005, MNRAS, 361, 415
Cooray, A., & Sheth, R. 2002, Phys. Rept., 372, 1
Croton, D. J., et al., 2004, MNRAS, 352, 1232
Eisenstein, D. J., et al., 2001, AJ, 122, 2267
Eisenstein, D. J., et al., 2005, ApJ, 633, 560
Folkes, S., et al. 1999, MNRAS, 308, 459
Fosalba, P., Pan, J., Szapudi, I., 2005, astro-ph/0504305
Frieman, J. A., & Gaztañaga, E. 1999, ApJ, 521, L83
Fukugita, M., Ichikawa, T., Gunn, J.E., Doi, M., Shimasaku, K., & Schneider, D.P. 1996, AJ, 111, 1748
Gaztañaga, E., & Scoccimarro, R. 2005, MNRAS, 361, 824 (GS05)
Gaztañaga, E., Norberg, P., Baugh, C. M., & Croton, D. J. 2005, MNRAS, 921
Gray, A. G., Moore, A. W., Nichol, R. C., Connolly, A. J., Genovese, C., & Wasserman, L. 2004, ASP Conf. Ser. 314: Astronomical Data Analysis Software and Systems (ADASS) XIII, 314, 249
Groth, E. J., & Peebles, P. J. E., 1977, ApJ, 217, 385
Gunn, J.E., et al. 1998, AJ, 116, 3040
Gunn, J.E., et al. 2006, AJ, 131, 2332
Hogg, D.W., Finkbeiner, D.P., Schlegel, D.J., and Gunn, J.E. 2001, AJ, 122, 2129
Ivezic, Z., et al. 2004, AN, 325, 583
Jing, Y. P., & Börner, G. 1998, ApJ, 503, 37
Jing, Y. P., & Börner, G. 2004, ApJ, 607, 140
Kravtsov., A. V., Berlind, A. A., Wechsler, R. H., Klypin A. A., Gottloeber S., Allgood B. & Primack J. R., 2004, ApJ, 609, 35
Marin, F., Wechsler, R., Nichol, R. C., 2006, in preparation.
Moore, A. W., et l. 2001, Mining the Sky, 71

Navarro, J. F., Frenk, C. S., & White, S. D. M. 1997, ApJ, 490, 493
Nichol, R. C. et al. 2003, Statistical Challenges in Astronomy, 265
Nichol, R. C. et al. 2005, ASP Conference Series, Vol. XXX, C. Gabriel, C. Arviset, D. Ponz and E. Solano (astro-ph/0510844)
Nichol, R. C. et al. 2006, MNRAS, 368, 1507
Nishimichi, T., et al. 2006, PASJ, submitted (see astro-ph/0609740)
Peebles, P. J. E. 1980, Large Scale Structure in the Universe, Princeton University Press
Pier, J.R., Munn, J.A., Hindsley, R.B., Hennessy, G.S., Kent, S.M., Lupton, R.H., and Ivezic, Z. 2003, AJ, 125, 1559
Scoccimarro, R., Sheth, R. K., Hui, L., & Jain, B. 2001, ApJ, 546, 20
Scranton, R., et al. 2002, ApJ, 579, 48
Sefusatti, E., Crocce, M., Pueblas, S., Scoccimarro, R., 2006, Phys.Rev. D74, 023522
Seo H-J, Eisenstein, D. J., 2005, ApJ, 633, 575
Sheth, R. K., & Tormen, G. 1999, MNRAS, 308, 119
Sheth, R. K., & Diaferio, A. 2001, MNRAS, 322, 901
Smith, J.A., et al 2002, AJ, 123, 2121
Stoughton, C., et al 2002, AJ, 123, 485
Strauss, M. A., et al. 2002, AJ, 124, 1810
Szapudi, I., Prunet, S., Pogosyan, D., Szalay, A. S., & Bond, J. R. 2001, ApJL, 548, L115
Szapudi, I. & Szalay, A. A., 1998, ApJ, 494, L41
Takada, M. & Jain, B., 2003, MNRAS, 335, 432
Tucker, D., et al. 2006, AN, in press
Wang, Y., Yang, X., Mo, H. J., van den Bosch, F. C., Chu, Y. 2004, MNRAS, 353, 287
York, D. G., et al. 2000, AJ, 120, 1579
Verde, L., et al., 2002, MNRAS, 335, 432
Zehavi, I. et al., 2005, ApJ, 630, 1
Zheng, Z., Weinberg, D. H., astro-ph/0512071

APPENDIX A: THE 3PCF DATA

Following tables contain the values of the data points in the figure 2. The errors given here are our estimates from jack-knife resampling and represent the diagonal elements of the covariance matrix The column named 'DDD' gives the number of triplets in the data for the corresponding bin.

Table A1. 3PCF measurements for $3.7 s < 4.3 h^{-1}$Mpc

θ_{min}	θ_{max}	DDD	$\zeta(s,q,\theta)$	σ_ζ	$Q_z(s,q,\theta)$	σ_{Q_z}	DDD	$\zeta(s,q,\theta)$	σ_ζ	$Q_z(s,q,\theta)$	σ_{Q_z}	DDD	$\zeta(s,q,\theta)$	σ_ζ	$Q_z(s,q,\theta)$	σ_{Q_z}
		$0.9 < q < 1.1$					$1.9 < q < 2.1$					$2.9 < q < 3.1$				
0.020	0.040	19	426.397	822.366	0.707	0.264	172	65.937	8.766	0.835	0.117	417	21.340	2.246	0.841	0.090
0.060	0.080	37	350.639	74.754	0.748	0.118	201	57.863	8.052	0.762	0.111	460	20.422	2.188	0.826	0.091
0.100	0.120	57	244.196	65.802	0.755	0.168	262	54.209	6.128	0.770	0.094	509	17.955	1.948	0.753	0.078
0.140	0.160	61	157.611	30.985	0.576	0.098	326	46.236	4.215	0.722	0.072	613	17.547	1.629	0.771	0.063
0.180	0.200	59	106.098	23.236	0.467	0.096	368	39.005	3.510	0.670	0.062	687	15.411	1.730	0.710	0.058
0.220	0.240	81	111.398	12.279	0.583	0.044	372	31.463	3.510	0.598	0.059	777	14.387	1.362	0.704	0.048
0.260	0.280	92	109.073	9.469	0.640	0.043	376	27.098	3.910	0.569	0.074	839	13.126	1.161	0.679	0.040
0.300	0.320	67	101.938	13.075	0.664	0.081	362	23.166	2.796	0.527	0.057	832	11.734	1.176	0.634	0.040
0.340	0.360	66	83.169	5.983	0.601	0.043	331	20.863	2.423	0.511	0.046	785	10.943	1.255	0.618	0.050
0.380	0.400	110	76.032	8.263	0.604	0.060	269	19.024	2.600	0.497	0.059	683	10.023	1.096	0.595	0.044
0.420	0.440	135	65.968	7.125	0.569	0.060	240	17.607	3.003	0.493	0.074	541	9.116	1.216	0.564	0.058
0.460	0.480	155	62.264	9.201	0.573	0.081	349	17.588	2.720	0.524	0.067	611	9.063	1.349	0.583	0.067
0.500	0.520	157	55.097	7.701	0.538	0.061	432	17.541	2.915	0.552	0.076	791	8.986	1.331	0.599	0.070
0.540	0.560	166	53.064	8.110	0.548	0.064	525	18.929	3.170	0.624	0.086	941	8.833	1.213	0.611	0.066
0.580	0.600	203	62.454	6.711	0.670	0.053	573	18.740	2.889	0.639	0.083	1057	8.887	1.045	0.636	0.057
0.620	0.640	214	62.468	6.236	0.692	0.057	619	19.918	2.256	0.697	0.068	1128	9.095	0.926	0.669	0.048
0.660	0.680	222	65.282	6.752	0.745	0.072	623	20.388	2.819	0.727	0.091	1126	8.981	0.809	0.679	0.043
0.700	0.720	214	63.369	7.396	0.738	0.076	604	20.587	2.497	0.752	0.081	1105	9.184	0.868	0.706	0.047
0.740	0.760	204	62.464	7.932	0.743	0.088	572	20.626	2.295	0.768	0.074	1040	9.115	0.905	0.715	0.053
0.780	0.800	194	62.797	9.055	0.756	0.105	552	21.731	2.263	0.823	0.078	971	9.186	0.785	0.734	0.045
0.820	0.840	181	63.600	9.996	0.778	0.122	513	22.037	2.181	0.843	0.078	901	9.205	0.596	0.743	0.037
0.860	0.880	174	65.524	10.185	0.809	0.127	466	21.649	2.280	0.836	0.081	831	9.166	0.614	0.750	0.042
0.900	0.920	163	65.106	9.223	0.813	0.120	436	21.718	2.307	0.844	0.088	780	9.236	0.685	0.761	0.048
0.940	0.960	158	66.026	9.590	0.828	0.127	411	21.396	2.308	0.836	0.091	756	9.490	0.729	0.784	0.053
0.980	1.000	155	66.075	10.032	0.829	0.132	405	21.764	2.304	0.851	0.092	747	9.695	0.776	0.802	0.057

Table A2. 3PCF measurements for $6.9s < 7.1h^{-1}$Mpc

θ_{min}	θ_{max}	DDD	$\zeta(s,q,\theta)$	σ_ζ	$Q_z(s,q,\theta)$	σ_{Q_z}	DDD	$\zeta(s,q,\theta)$	σ_ζ	$Q_z(s,q,\theta)$	σ_{Q_z}	DDD	$\zeta(s,q,\theta)$	σ_ζ	$Q_z(s,q,\theta)$	σ_{Q_z}
		$0.9 < q < 1.1$					$1.9 < q < 2.1$					$2.9 < q < 3.1$				
0.020	0.040	16	102.117	27.123	0.589	0.170	92	13.319	2.875	1.097	0.263	92	4.767	0.936	1.401	0.326
0.060	0.080	26	59.691	21.345	0.538	0.182	106	10.485	1.878	0.909	0.180	106	4.352	0.865	1.305	0.285
0.100	0.120	35	46.977	14.803	0.601	0.179	121	7.680	1.334	0.714	0.138	121	3.546	0.858	1.103	0.274
0.140	0.160	42	32.994	6.888	0.583	0.113	128	5.363	0.752	0.563	0.090	128	2.817	0.581	0.922	0.197
0.180	0.200	42	22.151	4.311	0.495	0.097	133	4.584	1.028	0.546	0.103	133	2.203	0.500	0.761	0.141
0.220	0.240	57	24.984	4.697	0.707	0.121	132	3.657	0.820	0.488	0.104	132	2.054	0.407	0.752	0.119
0.260	0.280	64	22.355	5.427	0.755	0.168	121	2.066	0.637	0.301	0.096	121	1.782	0.571	0.681	0.177
0.300	0.320	44	16.826	6.547	0.672	0.250	132	2.265	0.652	0.365	0.117	132	1.604	0.515	0.648	0.179
0.340	0.360	36	9.797	3.850	0.435	0.164	142	2.802	0.907	0.491	0.159	142	1.343	0.491	0.572	0.188
0.380	0.400	59	9.263	2.161	0.452	0.103	125	3.130	0.847	0.590	0.161	125	0.865	0.350	0.391	0.149
0.420	0.440	67	9.646	1.771	0.531	0.090	100	3.045	0.760	0.625	0.149	100	0.642	0.380	0.306	0.181
0.460	0.480	73	9.094	2.244	0.545	0.120	165	3.306	0.930	0.725	0.188	165	0.525	0.336	0.264	0.167
0.500	0.520	69	5.851	1.552	0.366	0.096	174	2.669	0.950	0.614	0.196	174	0.654	0.234	0.347	0.114
0.540	0.560	82	7.607	1.217	0.496	0.082	160	1.743	0.685	0.420	0.153	160	0.970	0.325	0.546	0.173
0.580	0.600	83	7.101	1.528	0.486	0.118	177	2.225	0.673	0.555	0.150	177	1.085	0.435	0.630	0.220
0.620	0.640	96	8.468	1.907	0.602	0.152	185	2.140	0.629	0.549	0.153	185	1.135	0.458	0.676	0.217
0.660	0.680	91	6.967	1.670	0.510	0.132	211	2.857	0.686	0.745	0.177	211	1.013	0.431	0.615	0.217
0.700	0.720	112	9.696	1.912	0.729	0.169	236	3.570	0.931	0.962	0.238	236	1.095	0.304	0.682	0.157
0.740	0.760	121	11.390	2.085	0.871	0.183	232	3.577	0.714	0.985	0.210	232	1.247	0.339	0.787	0.197
0.780	0.800	112	11.276	1.913	0.877	0.173	231	4.198	0.791	1.180	0.247	231	1.328	0.226	0.850	0.126
0.820	0.840	105	11.677	2.097	0.920	0.191	210	4.418	0.998	1.258	0.319	210	1.552	0.308	1.015	0.213
0.860	0.880	95	11.574	2.398	0.923	0.212	184	4.519	1.055	1.307	0.337	184	1.720	0.404	1.115	0.263
0.900	0.920	92	13.354	2.652	1.079	0.237	156	4.387	0.899	1.270	0.296	156	1.800	0.358	1.175	0.221
0.940	0.960	89	14.399	3.144	1.170	0.280	143	4.734	0.972	1.380	0.328	143	1.906	0.450	1.245	0.281
0.980	1.000	84	14.289	3.163	1.165	0.284	135	4.783	1.031	1.392	0.344	135	1.934	0.387	1.267	0.247

Table A3. 3PCF measurements for $9.9s < 10.1h^{-1}$Mpc

θ_{min}	θ_{max}	DDD	$\zeta(s,q,\theta)$	σ_ζ	$Q_z(s,q,\theta)$	σ_{Q_z}	DDD	$\zeta(s,q,\theta)$	σ_ζ	$Q_z(s,q,\theta)$	σ_{Q_z}	DDD	$\zeta(s,q,\theta)$	σ_ζ	$Q_z(s,q,\theta)$	σ_{Q_z}
		$0.9 < q < 1.1$					$1.9 < q < 2.1$					$2.9 < q < 3.1$				
0.020	0.040	40	35.077	9.336	0.565	0.115	183	3.802	0.736	1.167	0.221	220	0.999	0.297	1.203	0.354
0.060	0.080	62	21.049	4.319	0.536	0.102	228	3.087	0.627	0.993	0.191	279	0.983	0.230	1.223	0.289
0.100	0.120	95	19.423	2.093	0.753	0.068	281	2.286	0.359	0.804	0.126	362	0.882	0.176	1.140	0.240
0.140	0.160	82	8.381	2.189	0.476	0.119	312	1.526	0.357	0.596	0.142	422	0.657	0.157	0.898	0.228
0.180	0.200	98	7.727	1.858	0.600	0.142	308	1.089	0.420	0.480	0.191	469	0.524	0.136	0.785	0.238
0.220	0.240	103	5.876	1.161	0.585	0.116	318	1.127	0.513	0.566	0.260	458	0.385	0.137	0.633	0.250
0.260	0.280	96	3.095	1.266	0.373	0.149	334	0.952	0.419	0.538	0.243	485	0.440	0.097	0.777	0.219
0.300	0.320	64	1.132	0.921	0.168	0.133	330	0.663	0.229	0.414	0.148	513	0.488	0.107	0.897	0.205
0.340	0.360	85	2.739	0.841	0.449	0.127	310	0.382	0.186	0.260	0.123	503	0.315	0.112	0.624	0.218
0.380	0.400	125	2.331	0.692	0.426	0.124	259	0.351	0.370	0.256	0.271	467	0.311	0.175	0.648	0.348
0.420	0.440	147	2.593	0.775	0.518	0.158	228	0.573	0.508	0.455	0.411	361	0.426	0.226	0.928	0.444
0.460	0.480	151	1.855	0.549	0.398	0.117	323	0.168	0.360	0.143	0.310	416	0.359	0.183	0.840	0.364
0.500	0.520	166	1.702	0.746	0.397	0.177	387	0.360	0.229	0.333	0.218	578	0.417	0.156	1.006	0.295
0.540	0.560	164	1.100	0.800	0.271	0.200	423	0.546	0.157	0.535	0.151	610	0.332	0.134	0.829	0.305
0.580	0.600	194	1.881	0.569	0.487	0.152	489	0.939	0.166	0.950	0.158	634	0.332	0.118	0.864	0.272
0.620	0.640	201	1.672	0.647	0.449	0.179	506	0.963	0.244	1.007	0.245	622	0.241	0.101	0.659	0.239
0.660	0.680	220	2.173	0.579	0.597	0.164	528	1.109	0.221	1.193	0.269	639	0.225	0.125	0.642	0.320
0.700	0.720	248	2.691	0.668	0.758	0.188	548	1.143	0.248	1.254	0.307	672	0.346	0.158	0.985	0.385
0.740	0.760	246	2.728	0.592	0.782	0.164	528	1.033	0.327	1.147	0.381	694	0.460	0.171	1.374	0.429
0.780	0.800	239	3.123	0.647	0.912	0.188	492	1.051	0.326	1.201	0.390	650	0.443	0.177	1.355	0.464
0.820	0.840	230	3.508	0.730	1.040	0.211	427	0.904	0.307	1.046	0.355	598	0.547	0.221	1.683	0.585
0.860	0.880	205	3.482	0.724	1.045	0.210	388	1.078	0.320	1.259	0.381	524	0.597	0.245	1.831	0.651
0.900	0.920	185	3.589	0.763	1.088	0.224	330	1.031	0.247	1.208	0.291	451	0.630	0.239	1.939	0.660
0.940	0.960	168	3.669	0.803	1.117	0.235	294	1.142	0.275	1.356	0.314	391	0.595	0.256	1.852	0.750
0.980	1.000	162	3.794	0.879	1.157	0.257	265	1.002	0.339	1.198	0.402	361	0.588	0.260	1.834	0.755